Inorganic Chemistry Communications 162 (2024) 112230

Contents lists available at ScienceDirect

Inorganic Chemistry Communications

journal homepage: www.elsevier.com/locate/inoche

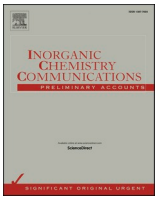

Short communication

Optical properties and Judd-Ofelt analysis of a novel Red-Emitting monoclinic $Li_3Ba_2Gd_3(WO_4)_8$: Eu^{3+} phosphor

Zhonghuan Zhang [a], Abir Douzi [a,b], Sami Slimi [a], Eduard Madirov [c], Amal Arouri [d], Víctor Llamas [e], Josep Maria Serres [e], Rosa Maria Solé [a], Magdalena Aguiló [a], Francesc Díaz [a], Ezzedine Ben Salem [b], Andrey Turshatov [c], Bryce S. Richards [c], Xavier Mateos [a,f,*]

[a] Universitat Rovira i Virgili (URV), Física i Cristal·lografia de Materials (FiCMA), Marcel·li Domingo 1, 43007, Tarragona, Spain
[b] I.P.E.I. of Monastir, Unit of Materials and Organic Synthesis, University of Monastir 5019, UR17ES31, Tunisia
[c] Institute of Microstructure Technology, Karlsruhe Institute of Technology, Hermann-von-Helmholtz-Platz 1, 76344 Eggenstein-Leopoldshafen, Germany
[d] University of Tunis El Manar, Faculty of Sciences of Tunis, Laboratory of Materials, Crystal Chemistry and Applied Thermodynamics, 2092 El Manar II, Tunis, Tunisia
[e] Eurecat, Centre Tecnològic de Catalunya, Advanced Manufacturing Systems Unit (AMS), Marcel·lí Domingo 2, 43007 Tarragona, Spain
[f] Serra Húnter Fellow

ARTICLE INFO

Keywords:
Quaternary tungstates
Europium ions
Crystal structure
Luminescence
Judd-Ofelt
wLEDs

ABSTRACT

Red-emitting $Li_3Ba_2Gd_3(WO_4)_8$: x at.% Eu^{3+} ($0.5 \leq x \leq 10$) phosphors were effectively produced using a conventional solid-state reaction method at high temperature in air atmosphere. The phosphors exhibited monoclinic crystalline structure with the C2/c space group and 2/m point group. The unit cell parameters determined from the Rietveld refinement for 3 at.% doped sample are a = 5.2149(4) Å, b = 12.7447(1) Å, c = 19.2058(3) Å, $\alpha = \gamma = 90°$, β = a^c = 91.9315(1)° and V_{calc} = 1275.748(2) Å^3. Photoluminescence spectra, lifetimes, colour coordinates and purity, and temperature-dependent emission spectra have been systematically studied. Upon excitation at 395 nm, the phosphors displayed red emission with a peak centered at 614 nm, which was associated with the $^5D_0 \rightarrow {}^7F_2$ electrical dipolar transition of Eu^{3+}. At the same time, the influence of different Eu^{3+} ion concentration on the photoluminescence intensity is also discussed. The optimal concentration of Eu^{3+} ions in $Li_3Ba_2Gd_3(WO_4)_8$ was found to be 3 at.%. The mechanism behind concentration quenching was ascribed to dipole–dipole interactions, and the critical distance for energy transfer among Eu^{3+} ions was determined to be 7.409 Å. The Judd–Ofelt theory was utilized to assess the intensity parameters and radiative properties. The fluorescence decay times were also determined for the different concentration levels of Eu^{3+} cations. The chromatic coordinates of $Li_3Ba_2Gd_3(WO_4)_8$: Eu^{3+} were found to be (0.653, 0.345), closely resembling the standard red light (0.670, 0.330) and demonstrated high colour purity (98.42 %) under excitation at 395 nm. Moreover, the phosphors $Li_3Ba_2Gd_3(WO_4)_8$: Eu^{3+} exhibited favorable thermal stability, characterized by an activation energy of 0.219 eV. The aforementioned findings indicate that the phosphors $Li_3Ba_2Gd_3(WO_4)_8$ doped with Eu^{3+} have the potential to function as a red-emitting phosphor in near-ultraviolet-driven white light-emitting diodes.

1. Introduction

In 1997, the initial white light-emitting diodes (wLEDs) became commercially available [1]. In our contemporary society, with the rise of digitalization, wLEDs are gaining global recognition for their exceptional qualities, such as high brightness, eco-friendliness, minimal energy consumption, superior luminous efficiency, and extended operational lifespan. They are therefore considered the next iteration of solid-state lighting tech [2–5]. In these white light-emitting diodes (wLEDs), luminescent materials, consisting of a host material and an activator ion, are used to transform the output of the blue LED chip into yellow light or a mixture of green and red light [6]. Rare earth (RE) ions, commonly used as activators, play a crucial role in display technology due to their outstanding luminescent properties. These properties translate into distinct emission bands characterized by 4f − 4f transitions, generally limited in free ions but partially allowed in a crystalline

* Corresponding author.
E-mail address: xavier.mateos@urv.cat (X. Mateos).

https://doi.org/10.1016/j.inoche.2024.112230
Received 9 December 2023; Received in revised form 6 February 2024; Accepted 19 February 2024
Available online 28 February 2024

host [7]. RE^{3+}-doped trivalent phosphors are of significant importance for solid-state illumination and radiation detection [8]. Exceptional stability, extended operational life, outstanding luminescent efficacy and environmental friendliness are key factors for the efficient use of phosphors in wLEDs. These characteristics are attained through the strategic incorporation of RE^{3+} dopants, a central focus of research efforts [9].

Currently, the predominant commercial red phosphors are rare-earth-doped nitrides and sulfides [10,11]. However, the complex synthesis conditions for RE-doped nitrides and the low stability of RE-doped sulfides affect their practical applications. Researchers are working to increase efficiency, improve synthesis conditions and the quality of phosphors. Among RE ions, the trivalent europium ion (Eu^{3+}), recognized as a highly effective activator, exhibits absorption in the UV/blue spectral range and can produce an intense red emission in the visible range [12,13]. For this reason, we chose to use the Eu^{3+} ion as an activator. Currently, Eu^{3+}-doped phosphors have been the subject of numerous reports, such as $NaBaBi_2(PO_4)_3$:Eu^{3+} [14], Sr_2LaNbO_6:Eu^{3+} [15], $SrMg_2La_2W_2O_{12}$:Eu^{3+} [16], $Gd_{4.67}Si_3O_{13}$:Eu^{3+} [17], $Ba_2Y_5B_5O_{17}$:Eu^{3+} [18], Y_2SiWO_8:Eu^{3+} [19], $LaSc_3(BO_3)_4$:Eu^{3+} [20], and Ba_2YMoO_6:Eu^{3+} [21]. The luminescence properties of these phosphors, which are based on different host materials, demonstrate that the host is also an important factor influencing the luminescence characteristics. Because of their high refractive index and stability, tungstates can serve as hosts for phosphors. Indeed, some tungstates can even produce self-activated emission [22–24]. Tungstate-based phosphors have the potential to facilitate efficient energy transfer between host and activators [25,26]. $Li_3Ba_2Gd_3(WO_4)_8$ (LBGW), one of the tungstates, has a monoclinic structure with a C2/c space group and unit cell parameters a = 5.217(3) Å, b = 12.763(9) Å, c = 19.204(13) Å, β = 91.928(17)° and Z = 2 [27]. To date, LBGW phosphors doped with RE^{3+} ions have been reported, including LBGW:Dy^{3+} [28], LBGW:Nd^{3+} [27], LBGW:Tb^{3+} [29] and LBGW:Er^{3+}/Yb^{3+} [30]. In light of these publications, it is demonstrated that LBGW is a promising host material for phosphors. Furthermore, no detailed description of the luminescence properties of LBGW:Eu^{3+} has been reported.

In this work, we studied the phase composition, microstructure and luminescence properties of a novel red-emitting Eu^{3+}-doped quaternary tungstate LBGW phosphors.

Furthermore, the Judd-Ofelt (JO) theory has been employed to investigate the local surroundings of Eu^{3+} ions within the LBGW host matrix. Ultimately, the aim of this article is to examine the spectroscopic and photometric attributes of LBGW: Eu^{3+} phosphors by exploring the photometric characteristics. These are clarified through the examination of photoluminescence spectra, highlighting the potential adaptability of the synthesized phosphor in diverse applications, including solid-state lighting (SSL) and electronic display devices.

2. Experimental

2.1. Synthesis and materials

Phosphor samples of LBGW: x at. % Eu^{3+} were synthesized using a conventional solid-state reaction method, covering a range of x values from 0.5 to 10 at. % Eu^{3+}. The doping level, expressed as x at. %, corresponds to the atomic percentage of Eu^{3+} ions replacing Gd^{3+} ions in the initial mixture. Precise quantities of the starting materials, including $BaCO_3$ (99.9 %, ChemPUR), Li_2CO_3 (>99 %, VWR Chemicals), Gd_2O_3 (99.99 %, Treibacher AG), Eu_2O_3 (99.99 %, Treibacher AG), and WO_3 (>99 %, Honeywell Fluka), were measured and subsequently mixed thoroughly using an agate mortar and pestle to achieve uniform blends. The powder obtained were subsequently placed in an alumina crucible and subjected to an initial preheating step at 700 °C for 24 h in an oxygen-rich environment to eliminate CO_2 gas. Subsequently, the grinding procedure was reiterated, and the samples were maintained at 900 °C for another 24-hour duration to ensure thorough reaction and the acquisition of single-phase LBGW: Eu^{3+} samples. Finally, the samples are gently cooled in the oven to room temperature.

2.2. Measurements

X-ray diffraction (XRD) data for the synthesized powder were obtained with the aid of X-ray diffractometer D8 Advance of Bruker AXS that featured a vertical θ-θ goniometer and CuK-α (with a wavelength of λ = 0.154060 nm) radiation. Scans were performed with a rate of 0.02° within the 2θ range of 10–80°, and the X-rays were detected using a Lynx Eye PSD detector with an opening angle of 2.94°. Raman spectra were captured using a Renishaw InVia confocal Raman microscope that featured an edge filter, a 50 × objective lens, and an Ar^+ ion laser with an excitation wavelength of 514 nm. Differential thermal analysis (DTA) was conducted employing a MOM Q-1500 D derivatograph, utilizing a Platinum-Rhodium thermocouple and a platinum crucible, with cooling and heating rates set at 15 °C/min, and analysis took place under a nitrogen flow of 140 cm^3/min.

The morphological features of the products were investigated through scanning field emission electron microscopy (FESEM), using an FEI Quanta 600 instrument. Samples compositions were identified by means of energy-dispersive X-ray spectroscopy (EDX) with the same FESEM apparatus, linked to an Oxford Inca 3.0 microanalyzer.

The reflectance spectra at ambient temperature were captured employing a UV–visible-IR spectrophotometer Varian CARY 5000. Excitation and emission spectra were measured by means of a spectrofluorometer (FS5, Edinburgh Instruments) fitted with an internal xenon lamp for excitation. Luminescence lifetime was monitored using a photomultiplier tube (R928P, Hamamatsu) housed within a temperature-cooling enclosure (CoolOne, Horiba), and the luminescence wavelength was selected using a dual monochromator (Bentham, DTMS300). Temperature-dependent photoluminescence measurements were carried out with a spectrum analyzer (OSA, Ando AQ6315-E) for the detection, utilizing a 395 nm laser generated from a non-linear lithium triborate crystal using a femtosecond (fs)-790 nm Ti: sapphire pump as the excitation source, and a custom-made heating device in the temperature range spanning from 30 to 250 °C.

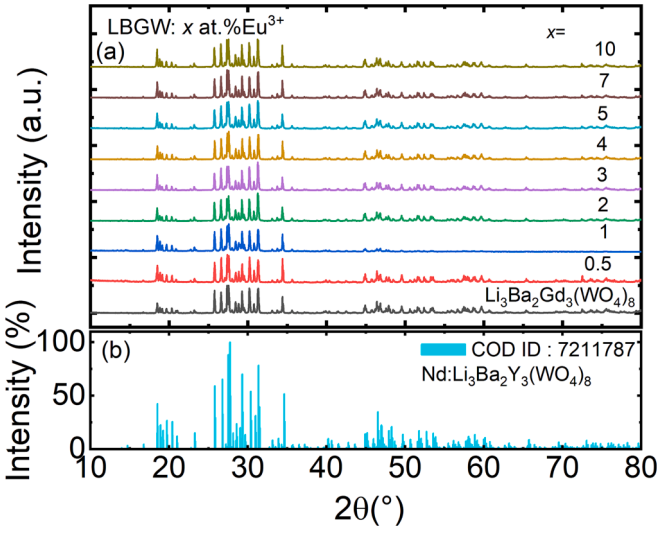

Fig. 1. (a) X-ray diffraction (XRD) patterns of LBGW with different doping concentrations of Eu^{3+} ions (0.5–10 %); (b) standard powder diffraction card of Nd: $Li_3Ba_2Y_3(WO_4)_8$, COD ID:7211787.

3. Results and discussion

3.1. Structural characteristics

The XRD patterns of the LBGW: x at. % Eu^{3+} phosphors (where x ranges from 0.5 to 10) are depicted in Fig. 1(a). These patterns closely match the data from the JCPDS card under reference #7211787, which corresponds to the $Li_3Ba_2Y_3(WO_4)_8$: Nd^{3+} crystal, as illustrated in Fig. 1 (b), serving as a reference standard. This similarity indicates the correct incorporation of Eu^{3+} ions into the $Li_3Ba_2Gd_3(WO_4)_8$ matrix. No additional diffraction peaks attributed to impurities are detected, confirming the single-crystalline phase nature of the synthesized phosphors. All the samples exhibit single phase-structure crystallized the monoclinic system, characterized by the C2/c space group and 2/m point group. Upon scrutinizing the positions of the diffraction peaks, it can be inferred that the inclusion of the Eu^{3+} activator ion did not alter the structural phase, as all observed peaks closely align with the standard LBGW host. This suggests that Eu^{3+} ions have effectively replaced Gd^{3+} ions (occupying sites at 8f) within the LBGW host matrix. This substitution is likely facilitated by the similarity in charges and ionic radii between Eu^{3+} (with a radius r of 1.066 Å and coordination number CN of 8) and Gd^{3+} (radius of 1.053 Å and CN = 8) [31].

To gain deeper insights into the structure of the phosphors, particularly regarding the integration of Eu^{3+} activator ions into the LBGW host matrix, we conducted a Rietveld refinement of the LBGW: 3 at.% Eu^{3+} compound using GSAS II software, as illustrated in Fig. 2. The initial refinement model was derived from the crystal data of $Li_3Ba_2Gd_3(WO_4)_8$ [27]. The calculated profile closely matches the experimental profile, and Table 1 provides a breakdown of the refinement parameters. The refinement results indicate the absence of any noticeable impurity phases, and the refined unit cell parameters are as follows: a = 5.2149(4) Å, b = 12.7447(1) Å, c = 19.2058(3) Å, α = γ = 90°, β = 91.9315(1)°, V_{calc} = 1275.748(2) $Å^3$, and the number of formula units Z = 4. The refinement successfully converged, yielding R_w = 7.78 % and a goodness-of-fit value (GOF) of 1.60. Upon comparing the crystallographic data of LBGW: 3 at.% Eu^{3+} with the pure LBGW host [27], it is confirmed that the unit cell volume has decreased slightly from 1277.9(15) $Å^3$ to 1275.748(2) $Å^3$. This phenomenon can be attributed to the smaller ionic radius of Eu^{3+} compared to Gd^{3+}, as previously observed. Additionally, the incorporation of Eu^{3+} activator ions into the matrix results in a noticeable increase in crystal density, from 7.147 to 7.527 g/cm^3, attributable to both the reduction in cell size and an increase in formula weight. Table 2 provides a summary of occupancy factors (O.F.), atomic coordinates, sites, and isotropic displacement parameters (B_{iso}) reported for the LBGW: 3 at.% Eu^{3+} sample.

A fragment of the LBGW: Eu^{3+} phosphor's structure is depicted in Fig. 3, showcasing its projection on the 2 crystallographic planes, namely a-b and b-c. Table 3 provides calculated interatomic distances for three different polyhedra: [Gd|Li1|Eu]O_8, [Ba]O_{10}, and [Li2]O_6. Within this structure, Ba^{2+} ions occupy the 4th sites and form a distorted polyhedron [Ba]O_{10} by coordinating with 10 oxygen atoms. The interatomic distances within this polyhedron range from 2.6082(9) to 3.2067 (8) Å. Li^+ cations, on the other hand, exist in two distinct crystallographic sites: 8f and 4e. The first site, known as Li1, is situated within the 8f sites and is distributed alongside the Gd^{3+}|Eu^{3+} cations. Each Gd|Li1|Eu is surrounded by 8 oxygen atoms, giving rise to a deformed polyhedron [Gd|Li1|Eu]O_8, with interatomic distances ranging from 2.2446 (1) to 2.7848(2) Å. The second site, referred to as Li2, is located in the 4e-type sites and is coordinated by six oxygen atoms, forming the polyhedron [Li2]O_6 with distances falling between 1.9907(5) and 2.3778(1) Å. The overall structure of the LBGW: x at.% Eu^{3+} phosphors comprises polyhedra such as [Ba]O_{10}, [Gd|Li1|Eu]O_8, and [Li2]O_6, which are interconnected through common oxygen atoms. The polyhedra adjacent to [Gd|Li1|Eu]O_8 create a two-dimensional layered structure aligned with the b-c plane, while the [Ba]O_{10} polyhedra connect to neighboring [Gd|Li1|Eu]O_8-[Gd|Li1|Eu]O_8 units, forming a 3-

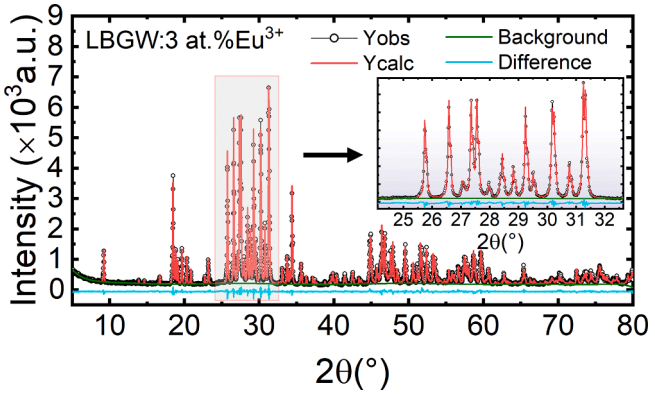

Fig. 2. Rietveld refinement plots for $Li_3Ba_2Gd_3(WO_4)_8$:3%Eu, the experimental profile-black dots; the calculated pattern-red line; the difference plot-blue line and the background-green line; *Inset*: zoomed view in the range between 25 and 32°.

Table 1
Crystallographic data and Rietveld refinement details for LBGW: 3 at.%Eu^{3+} sample.

Data	LBGW:3 at.%Eu^{3+}
Chemical formula	$Li_3Ba_2Gd_{2.91}Eu_{0.09}(WO_4)_8$
Crystal System	monoclinic
Space group (IT number, Z)	C 2/c (15, 2)
Laue Class	2/m
Calculated density (g/cm^3)	7.5272
Lattice constant a,b,c(Å)	5.2149(4), 12.7447(1), 19.2058(3)
α,β,γ(deg.)	90, 91.9315(1), 90
Volume($Å^3$)	1275.748(2)
2θ range (deg.)	10–80
2θ step	0.02
Radiations	Cu-Kα1 (λ = 1.5418 Å)
Refinement software	GSAS II software
Goodness of fit (GOF)	1.60
Rw	7.78 %

Table 2
Atomic coordinates, sites, occupancy factors (O.F) and isotropic displacement parameters B_{iso} ($Å^2$) LBGW: 3 at.% Eu^{3+} sample.

Atoms	sites	x/a	y/b	z/c	O.F	B_{iso}($Å^2$)
W1	8f	0.4887 (3)	0.4409 (3)	0.4057 (0)	1.000	1.342 (5)
W2	8f	0.5032 (7)	0.7435 (6)	0.3508 (3)	1.000	0.790 (3)
Ba	4e	1.0000 (0)	0.5317 (6)	0.2500 (0)	1.000	1.737 (9)
Gd|Li1|Eu	8f	1.0031 (0)	0.6468 (8)	0.4681 (8)	0.728|0.250|0.022	0.632 (2)
Li2	4e	0.5000 (0)	0.3220 (0)	0.2500 (0)	1.000	1.895 (3)
O1	8f	0.6329 (0)	0.4149 (0)	0.3263 (0)	1.000	2.921 (1)
O2	8f	0.2565 (5)	0.5433 (9)	0.4039 (0)	1.000	2.843 (7)
O3	8f	0.7726 (9)	0.4613 (1)	0.4459 (1)	1.000	2.264 (1)
O4	8f	0.3015 (3)	0.3350 (1)	0.4520 (9)	1.000	3.054 (9)
O5	8f	0.2218 (6)	0.7084 (9)	0.2847 (8)	1.000	2.737 (5)
O6	8f	0.7403 (9)	0.6493 (1)	0.3583 (0)	1.000	3.053 (4)
O7	8f	0.6617 (0)	0.8482 (7)	0.3280 (8)	1.000	2.580 (5)
O8	8f	0.2933 (5)	0.7472 (0)	0.4158 (5)	1.000	2.501 (2)

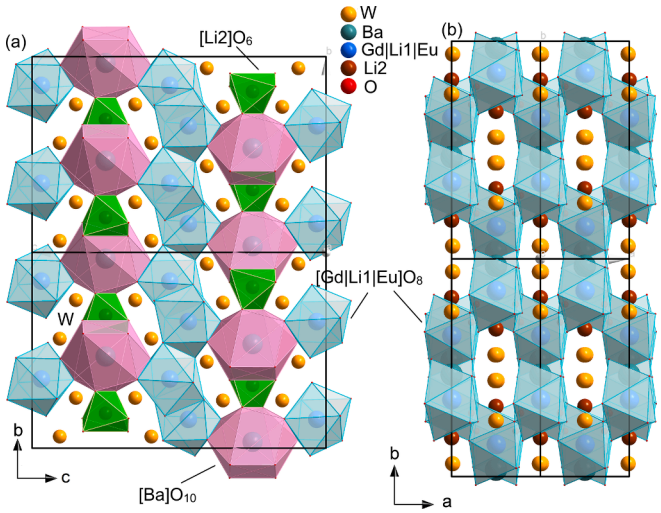

Fig. 3. Fragment of structure of LBGW: Eu^{3+} in projection to the (a) *b-c* plane and (b) *a-b* plane.

Table 3
Selected interatomic distances in LBGW: 3 at.% Eu^{3+}.

M−O distances (Å) × numbers		
[Gd|Li1|Eu] O_8	**[Li2] O_6**	**[Ba] O_{10}**
Gd|Li1|Eu-O	**Li2-O**	**Ba-O**
Gd|Li1|Eu-O8 = 2.2446(1) × 1	Li2-O1 = 1.9907(5) × 2	Ba-O5 = 2.6082(9) × 2
Gd|Li1|Eu-O4 = 2.2551(5) × 1	Li2-O5 = 1.9554(2) × 2	Ba-O1 = 2.8671(5) × 2
Gd|Li1|Eu-O3 = 2.2625(9) × 1	Li2-O7 = 2.3778(1) × 2	Ba-O7 = 2.8885(1) × 2
Gd|Li1|Eu-O3′ =2.4208(2) × 1		Ba-O6 = 2.9315(3) × 2
Gd|Li1|Eu-O6 = 2.4772(0) × 1		Ba-O2 = 3.2067(8) × 2
Gd|Li1|Eu-O4 = 2.6321(5) × 1		
Gd|Li1|Eu-O3'' =2.6804(6) × 1		
Gd|Li1|Eu-O8′ =2.7848(2) × 1		

dimensional network, resulting in a single-layer polyhedral structure. To ascertain the average crystallite size D, the Scherrer equation [32] is utilized:

$$D(nm) = \frac{K\lambda}{FWHM^{*}cos\theta} \quad (1)$$

where *D* represents the average crystallite size in nm, *K* presents the Scherrer constant, which is equal to 0.9, λ is the incident X-ray wavelength (Cu-Kα1; λ = 1.54060 Å), FWHM are the full-width at half maximum in radian, θ is related to the peak position (in radian). The average crystallite size of LBGW: *x* at.% Eu^{3+} phosphors with *x* varying between 0.5 and 10 at.% was determined to be ~ 63 nm.

See Fig. 4.(a) shows the DTA curves for LBGW:10 at.% Eu corresponding to the heating and cooling processes. From the curves, we observe that the synthesized samples show a single endothermic effect (during heating) and a single exothermic effect (during cooling). These effects present a strong and reversible character, which correspond to a congruent melting and crystallization. Furthermore, the initiation temperature of the fusion aligns closely with 1026 °C. As the samples were heated, we observed an endothermic peak at 1040 °C, indicating the melting process. This temperature level appears higher than that of the host matrix (LBGW: 1034 °C) [27]. Upon the samples' cooling, a detected exothermic peak at 1020 °C was associated with the crystallization of the monoclinic phase. The absence of further thermal effects

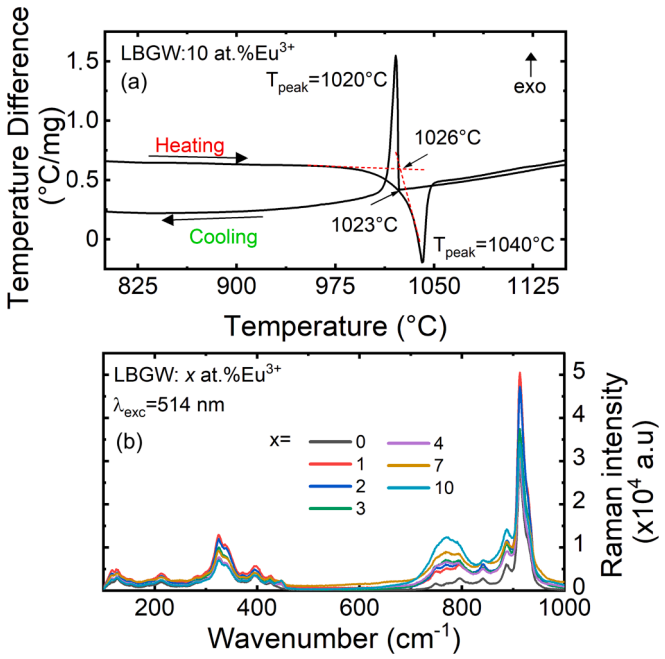

Fig. 4. DTA curves for LBGW: 10 at. %Eu^{3+}; (b) Raman spectra of $Li_3Ba_2Gd_3(WO_4)_8$:x at.%Eu phosphors, *x* = 0, 1, 2, 3, 4, 7 and 10 at.%.

indicates the lack of polymorphic phase transformations of the first type below the melting point of the composition.

The Raman spectra of LBGW: *x* at.% Eu^{3+} phosphors were obtained within the range of 100–1000 cm^{-1}, as illustrated in Fig. 4(b). It is apparent from these spectra that as the concentration of Eu^{3+} dopant ions increases, there are no significant alterations in the Raman profiles. These spectra closely resemble the profiles of pure LBGW (x = 0), affirming the formation of a single LBGW phase in our samples. Several distinct peaks are observed, including those centered at 913, 395, 337, and 325 cm^{-1}, attributed to the (W-O) stretching modes. Additionally, peaks at 887 and 841 cm^{-1} are assigned to (WOW) stretching modes. The peaks at 446 and 425 cm^{-1} correspond to bending modes δ(WOW), while those at 794 and 747 cm^{-1} are associated with bridge stretching modes ν(WOW). We also identify a peak at 213 cm^{-1}, which can be attributed to the translational modes of Gd^{3+} cations. Finally, two successive peaks at 115 and 125 cm^{-1} are identified as the out-of-plane (WOW) modes related to the translational modes of (W^{6+}, Gd^{3+}) ions [33,34]. The maximum phonon energy, denoted as $h\upsilon_{max}$, for LBGW: Eu^{3+} is 913 cm^{-1}.

3.2. Morphology and composition analysis

In Fig. 5(a), the scanning electron microscopy (SEM) image of LBGW: x at.% Eu^{3+} phosphor powder is presented. The resulting image illustrates that the particles exhibit irregular morphology and are agglomerated. The estimated size of the particles is likely in the micrometer range, approximately 5 μm, making it suitable for applications in white light-emitting diodes (wLEDs) [35]. Fig. 5(b,c) illustrates the EDX spectra for the $Li_3Ba_2Gd_3(WO_4)_8$ host and the synthesized powders LBGW: 3 at.% Eu^{3+}, respectively. These spectra demonstrate the existence of lithium (Li), barium (Ba), gadolinium (Gd), and tungsten (W) in both samples, with the additional presence of europium (Eu) in the samples doped with Eu^{3+} ions (x = 3 at.%). The EDX elemental mapping for the LBGW: 3 at.% Eu^{3+} sample is shown in Fig. 5(d) and its confirm that all the elements were homogeneously distributed over the entire analysed area.

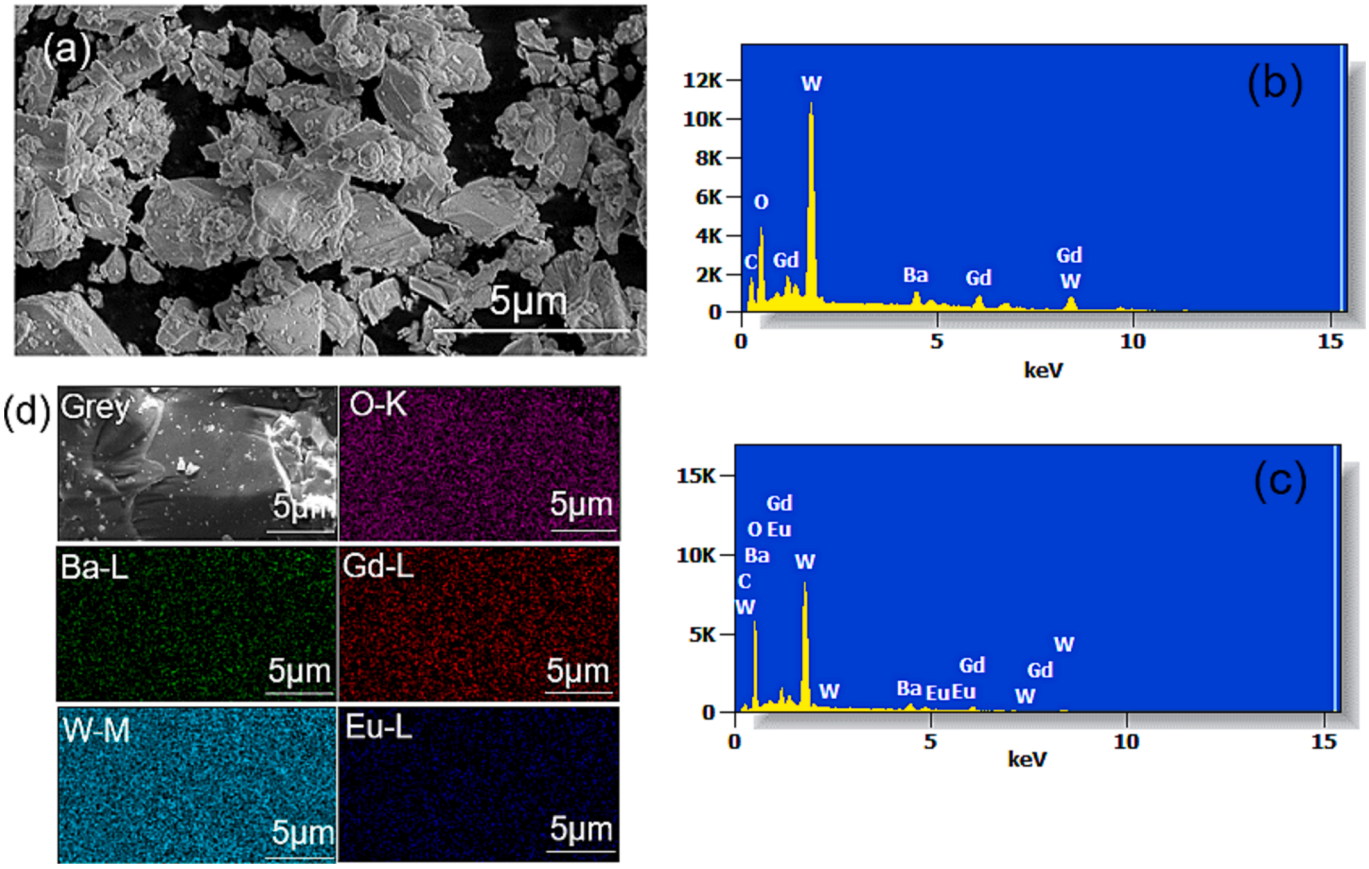

Fig. 5. (a) SEM image of LBGW: 3 at.%Eu^{3+} (b) Energy-dispersive X-ray (EDX) spectra for the host matrix (c) EDX spectra for LBGW: 3 at.%Eu^{3+} (d) EDX elemental mapping for the LBGW: 3 at.%Eu^{3+} samples.

3.3. Diffuse reflectance spectra

In comprehending the absorption and emission characteristics of the synthesized phosphors, a crucial optical parameter to observe is the diffuse reflectance spectrum. The diffuse reflectance spectra for the host samples LBGW and LBGW: 3 at.% Eu^{3+} are illustrated in Fig. 6(a). The expansive absorption band present in the 250–350 nm range is linked to the charge transfer band (CTB) involving O^{2-} ions transitioning to Eu^{3+}/W^{6+} [36]. The distinct bands observed are attributed to the intra 4f- 4f electronic transitions of the active Eu^{3+} ion. The peaks noted at about 464 and 535 nm are due to $^7F_0 \rightarrow {}^5D_2$ and $^7F_1 \rightarrow {}^5D_1$ of the Eu^{3+} ion. Moreover, we utilized the theory developed by Davis and Mott [37] to compute the optical absorption at the fundamental edge. This determination was made by considering the association between photon energy and the absorption coefficient for both direct and indirect optical transitions. This relationship can be written in the general form provided by:

$$\alpha(h\nu) = A\frac{(h\nu - E_g)^r}{h\nu} \quad (2)$$

where E_g denotes the optical band gap, $\alpha(h\nu)$ is the absorption coefficient, $h\nu$ represents the photon energy with A being a constant. For forbidden transitions, the value of r is 1/2. From the plot of the variation of $(\alpha h\nu)^2$ $(eV.cm^{-1})^2$ versus the energy (eV) (see Fig. 6(b)), we detect E_g = 2.78 eV for the host and E_g = 2.97 eV for the sample LBGW: 3 at.% Eu^{3+}. Consequently, the band gap energy levels rise as the concentration of dopant ions in the LBGW host lattice increases. This increase in energy levels can be attributed to the structural disruption that occurs within the host lattice due to the addition of Eu^{3+} dopant ions.

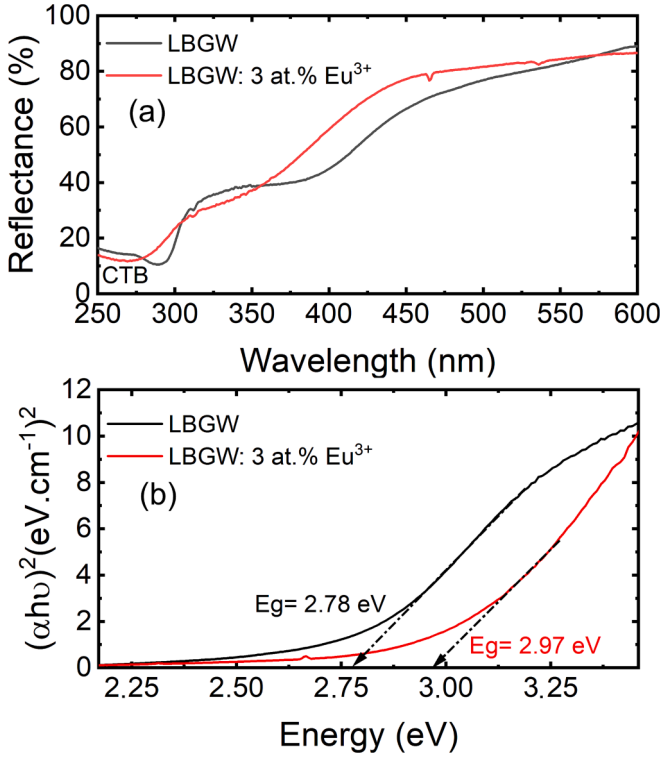

Fig. 6. (a) Diffuse reflection spectrum and (b) Tauc plots of undoped and for LBGW: 3 at.%Eu^{3+} samples.

3.4. Photoluminescence properties

Fig. 7(a) displays the photoluminescence (PL) and the photoluminescence excitation (PLE) spectra of LBGW:3 at.% Eu^{3+} phosphors. The PLE spectrum was measured under emission monitored at 614 nm, which corresponds to the $^5D_0 \rightarrow {}^7F_2$ transition of Eu^{3+} activator ions. The spectrum was formed in two parts: (i) a broad excitation band in the wavelength range between 250 and 300 nm, centered at 264 nm, which is the CTB between divalent O^{2-} anions and Eu^{3+}/W^{6+} cations, which corresponds to the electron transfer from the completely occupied 2p orbital of the O^{2-} to the empty 4f orbital states of Eu^{3+}/W^{6+} ions. This suggests that the energy absorbed in the near UV region is efficiently transmitted to Eu^{3+} ions via ligand–metal charge transfer absorption (CTB) [38]. In the CTB, the broadening of the peak is attributed to contributions from the intense lattice vibrations. The positioning of the CTB is influenced by factors such as the size, coordination number, charge of the cation, electronic affinity of the anion, and the coordination of cations around the O^{2-} ions [39]. (ii) a series of distinct and well-defined excitation peaks at 318, 361, 381, 395, 415, 464, 526, and 535 nm are associated with the 4f-4f transitions of the Eu^{3+} activator ions within the host arrays. These transitions can be identified as $^7F_0 \rightarrow {}^5H_6$, $^7F_0 \rightarrow {}^5D_4$, $^7F_0 \rightarrow {}^5L_7$, $^7F_0 \rightarrow {}^5L_6$, $^7F_0 \rightarrow {}^5D_3$, $^7F_0 \rightarrow {}^5D_2$, $^7F_0 \rightarrow {}^5D_1$, and $^7F_1 \rightarrow {}^5D_1$, respectively [40–42]. Among the observed LPE peaks, it is clear that the most notable excitation peak is positioned at a wavelength of 395 nm, this particular peak exhibits slightly greater intensity compared to the one in the blue region at 464 nm. These two peaks are well-suited for exciting the phosphors using commercially accessible InGaN-based near-UV and GaN-based blue LED chips, respectively.

The PL emission spectra of the LBGW: 3at.% Eu^{3+} sample were studied using two different excitation wavelengths: 264 nm (CTB) and 395 nm (Eu^{3+} direct). As there is no detectable emission from the WO_4^{2-} group, this suggests the presence of phenomena associated with "host-sensitized" energy transfer [43,44]. The emission intensity under 395 nm excitation ($^7F_0 \rightarrow {}^5L_6$) is the highest, and five characteristic emission peaks were found at 591, 614, 654 and 701 nm, mapping respectively to the $^5D_0 \rightarrow {}^7F_1$, $^5D_0 \rightarrow {}^7F_2$, $^5D_0 \rightarrow {}^7F_3$ and $^5D_0 \rightarrow {}^7F_4$ transitions of Eu^{3+} ions. The Eu^{3+} ion in the LBGW host, belonging to the C2/c space group, is surrounded by eight oxygen atoms, exhibiting no inversion symmetry, also known as S4 point symmetry, as indicated by reference [45]. Existing studies propose that introducing A^{2+} ions as aliovalent dopants for Eu^{3+} might lead to a local distortion in the S4 symmetry at the Eu^{3+} site [46]. Based on the outcomes of the structure refinement, it is established that Eu^{3+} ions occupy the same crystallographic positions as Li^+ and Gd^{3+}. The lack of $^5D_0 \rightarrow {}^7F_0$ emission at 582 nm, which is exclusive to sites with C_s, C_n, or C_{nv} symmetry, further reinforces this point [47]. A depiction of energy levels, demonstrating the energy transfer process between WO_4^{2-} and Eu^{3+} ions within LBGW, can be seen in Fig. 7(b). Generally, WO_4^{-2} groups capture photon energy and subsequently relay it to Eu^{3+}, causing Eu^{3+} to emit red light effectively [48,49]. Upon exposure to near-ultraviolet (n-UV) light, electrons are propelled to the WO_4^{2-} charge transfer band (CTB), then descend to lower energy states via non-radiative processes. Afterwards, energy is released from the ligands to the metallic ions (Eu^{3+}), exciting the electrons to elevated energy states [50]. Finally, through a radiative transition, the excited electrons ($^5D_0$) revert to the ground state ($^7F_1$, $^7F_2$, $^7F_3$, and $^7F_4$), giving off intense red light.

To fulfill the goal of examining the luminescent properties of the prepared samples, we investigated the impact of Eu^{3+} dopant concentration on the luminescence intensity of LBGW: *x* at.% Eu^{3+} phosphors with *x* varying from 0.5 to 10. The emission spectra were recorded within the 570–715 nm range while being excited at 395 nm and at a room temperature of 25 °C, as depicted in Fig. 8(a). The configuration of these photoluminescence (PL) spectra remained consistent across various concentrations of Eu^{3+} activator ions, with the exception of the PL intensity, as illustrated in Fig. 8(b). This observation supports the conclusion that there is a singular Eu^{3+} emission center at the Gd^{3+} ion sites [51]. Notably, the PL intensity shows a gradual rise with increasing amounts of Eu^{3+} until it reaches a maximum and stabilizes at a value of

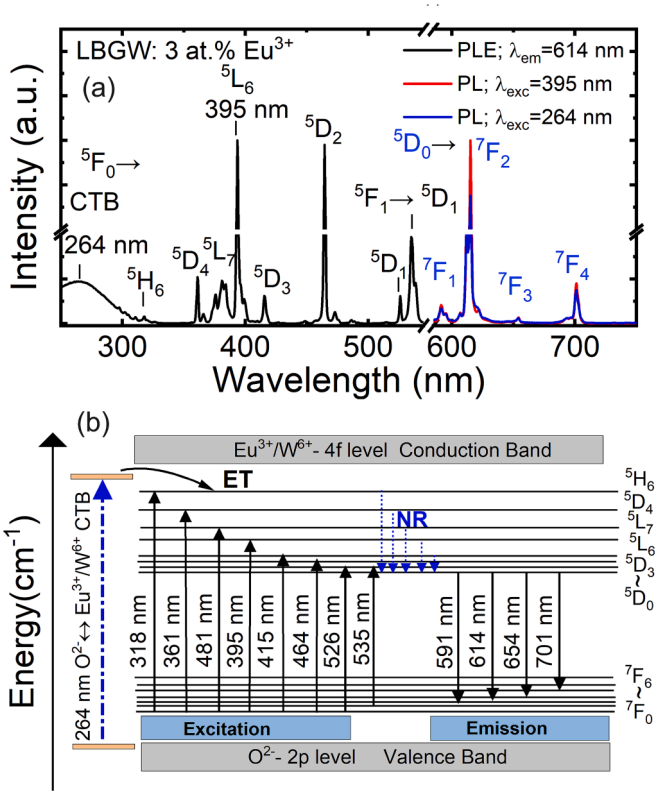

Fig. 7. (a) The photoluminescence excitation (PLE; λ_{em} = 614 nm) and photoluminescence (PL; λ_{exc} = 264 nm and 395 nm) spectra of for LBGW: 3 at.% Eu^{3+} phosphors. (b) The energy level diagram.

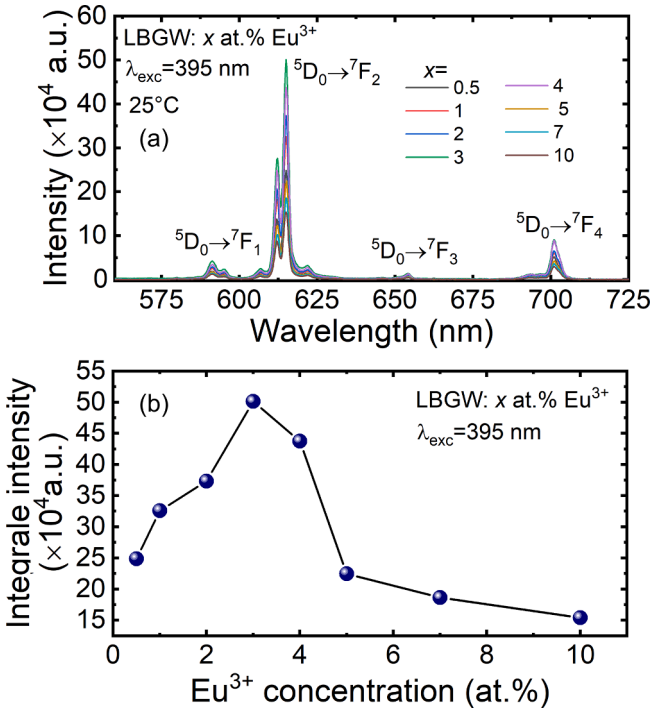

Fig. 8. (a) Emission spectra of LBGW: *x* at.% Eu^{3+} ($0.5 \leq x \leq 10$) phosphors, λ_{exc} = 395 nm; (b) PL as a function of Eu^{3+} concentration.

x = 3 at. % Eu^{3+}. Subsequently, a gradual decline in PL intensity is evident with a further increase in the content of Eu^{3+} ions.

Typically, concentration quenching is a phenomenon influenced by factors such as exchange interaction, multipole-multipole interaction, or radiation reabsorption. In the case of LBGW: Eu^{3+}, the bond angles involving (Eu-O-W) and (O-W-O) surpass 100 degrees, leading to a considerable separation between Eu^{3+} cations. This significant distance presents a considerable obstacle to energy transfer among the Eu^{3+} ions [52,53]. Conversely, the existence of isolated WO_4^{2-} groups within the structure effectively shields the Eu^{3+} activator ions from each other, forming a barrier to energy transfer between pairs of Eu^{3+} ions. Additionally, the non-radiative energy transfer process among Eu^{3+} ions is notably influenced by the critical transfer distance (*Rc*).This was determined using the concentration extinction method proposed by Blasse [54]:

$$R_c \approx \left(\frac{3V}{4\pi N \mathscr{X}_C}\right)^{\frac{1}{3}} \tag{3}$$

where *N* designates the number of lattice sites that are capable of being occupied by activator ions, *V* denotes the volume of the unit cell, and X_c represents the critical concentration of Eu^{3+} dopant ions. For LBGW: 3 at.% Eu^{3+}, we determined that: $V = 1277.9$ Å^3, $N = 2$, and $X_c = 3$ at. %, which implies that the critical distance R_c of the energy transfer is about 7.409 Å. When the critical distance is greater than 7.409 Å, the short-range exchange interaction loses its effectiveness. In our case, there is no overlap between the PLE and PL spectra, resulting in unlikely radiation reabsorption. Therefore, the quenching mechanism of Eu^{3+} ion concentration in our host matrix was dominated by multipole-multipole interactions. Three types of multipole electrical interactions are distinguished, namely dipole–dipole (d-d), quadrupole–quadrupole (q-q), and dipole-quadrupole (d-q). The luminescence intensity per activator ion can be described using Dexter's theory, as formulated in the following equation [55]:

$$\frac{I}{x} = K\left[1 + \beta(x)^{\frac{\theta}{3}}\right]^{-1} \tag{4}$$

Here, I represents the emission intensity, x signifies the concentration of Eu^{3+}, and β and *K* represent constants specific to the host under identical excitation conditions. The ratio I/x represents the luminescence intensity per activator concentration, with θ taking values of 6, 8, or 10, related to d-d, d-q, or q-q interactions, respectively [56]. Assuming that $\beta(x)$ is more than 1, the above equation can be restructured into the following form:

$$\log\frac{I}{x} = K' - \frac{\theta}{3}\log(x) \tag{5}$$

where $K' = \log K - \log\beta$, Fig. 9(a) shows the relationship between log(x) and log (I/x). This relationship results in a linear curve with a slope of −1.86254. Therefore, we can determine the value of θ from this slope, which may be 5.587. This value is about equal to 6, which suggests

that the phenomenon of non-radiative energy transfer between Eu^{3+} ions can be attributed to the d-d interaction in the LBGW: Eu^{3+} phosphors.

It can be noted that for all the samples, the intensity of the electric dipole transition (ED; $^5D_0 \rightarrow {}^7F_2$) at about 614 nm appears considerably more potent than the magnetic dipole transition (MD; $^5D_0 \rightarrow {}^7F_1$) at around 591 nm. The intense red emission ($^5D_0 \rightarrow {}^7F_2$) at 614 nm is observable for different Eu^{3+} concentration levels. The specific chemical environment surrounding Eu^{3+} within a host lattice influences the location of the f-f transition peak and the corresponding relative intensities. In accordance with the Judd-Ofelt theory, it is used to measure the symmetry of the environment surrounding the Eu^{3+} activator ions by examining the integrated emission intensity ratio (referred to as the R/O asymmetry ratio) between the $^5D_0 \rightarrow {}^7F_2$ transition and the $^5D_0 \rightarrow {}^7F_1$ transition.

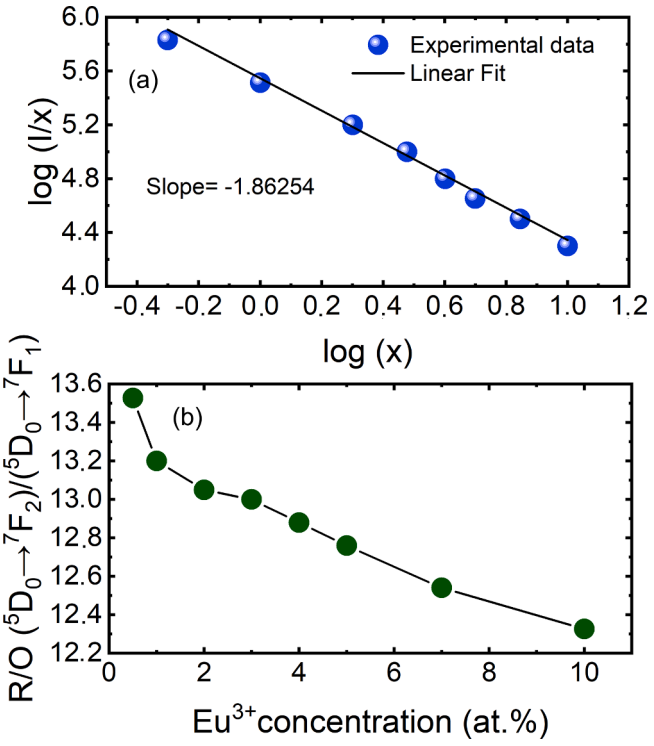

Fig. 9. (a) Dependence of log(I/x) on log(x) for of LBGW: *x* at.% Eu^{3+} with λ_{exc} = 395 nm (b) Asymmetry ratio values with different concentrations levels of Eu^{3+} ions.

As defined, to obtain the R/O asymmetry ratio of the $^5D_0 \rightarrow {}^7F_2$ transition relative to the $^5D_0 \rightarrow {}^7F_1$ transition should be determined as follows [57]:

$$\frac{R}{O} = \frac{I_{S_{D_O-{}^7F_2}}}{I_{S_{D_O-{}^7F_1}}} \tag{6}$$

In Fig. 9(b), a graph illustrates the emission ratio values of ($^5D_0 \rightarrow {}^7F_2$) / ($^5D_0 \rightarrow {}^7F_1$) transitions across various Eu^{3+} concentrations (x = 0.5 to 10 at.%), yielding calculated R/O values of 13.52, 13.20, 13.05, 13.01, 12.88, 12.76, 12.54, 12.32. Essentially, the asymmetry ratio values are consistently greater than 1, indicating the prevalence of the $^5D_0 \rightarrow {}^7F_2$ electric dipolar transition in the emission spectra of LBGW: Eu^{3+} phosphors. This suggests that Eu^{3+} occupies non-centrosymmetric positions within distorted cationic sites [58]. Similarly, it is clearly observed that with increasing Eu^{3+} ion concentration, the R/O values decrease, this fact means that the substitution of Gd^{3+} ions for Eu^{3+} ions hardly affect the local environment. The absence of central inversion of the Eu^{3+} ion is advantageous for producing a bright red phosphor of great colour purity.

3.5. Luminescence decay curves

The room temperature PL decay curves of LBGW: *x* at.%Eu^{3+} phosphors with different concentrations of Eu^{3+} under excitation at 395 nm and tracking at 614 nm are presented in Fig. 10(a). Decay curves for all cases are effectively modeled using a first-order exponential decay function. Consequently, the radiative relaxation lifetime of the $^5D_0$ level at different concentrations of Eu doping was determined using the following formula [40]:

$$I(t) = I_0 + Aexp(-\tfrac{t}{\tau}) \tag{7}$$

where I_0 and $I(t)$ are the intensities of luminescent emission at $t = 0$ and time *t*, respectively; *A* is a coefficient and τ is the lifetime. Based on the

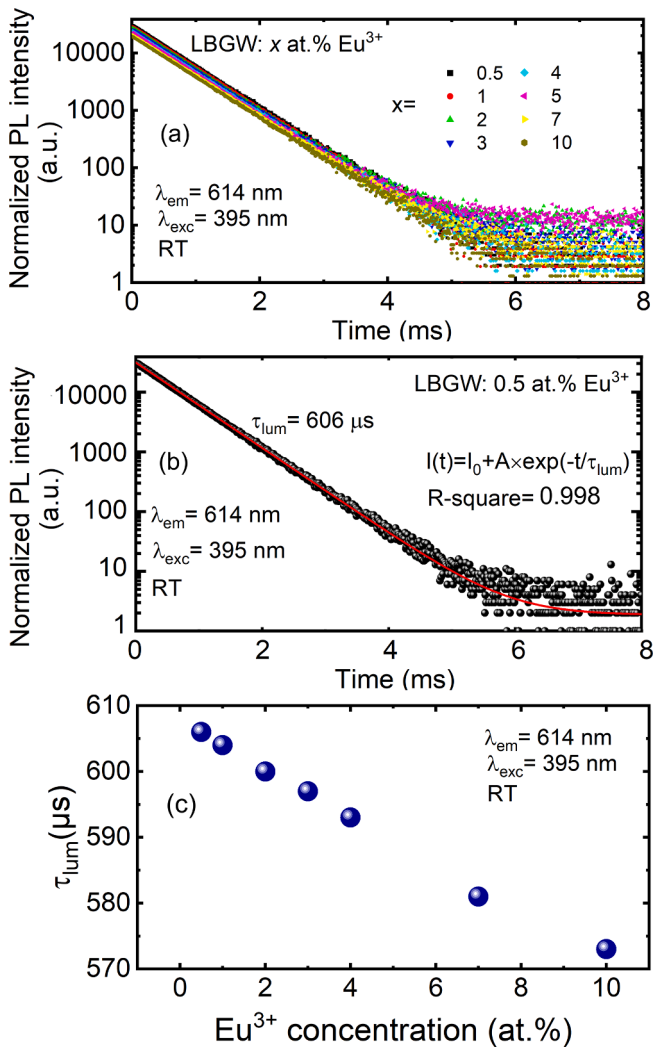

Fig. 10. (a) PL decay curves; (b) single exponential fit of the decay curve for the sample LBGW: 0.5 at.% Eu^{3+} (c) Luminescence lifetime as a function of doping concentration of LBGW: *x* at.% Eu^{3+} ($0.5 \leq x \leq 10$) phosphors excited at 395 nm and monitored at 614 nm.

previous equation, the lifetime was calculated as 606, 604, 600, 597, 593, 589, 581, and 573 μs for the synthesized phosphors with Eu^{3+} doping concentration of 0.5, 1, 2, 3, and 4, 5, 7, and 10 at.%, respectively. It can be noted that there is no significant variation in decay lifetime with increasing Eu^{3+} cation concentration, Fig. 10 (b). This implies that there was energy migration among the Eu^{3+} activators [59–62].

3.6. Judd–Ofelt theory analysis

Typically, the Judd-Ofelt (J-O) parameters are deduced by observing the absorption spectra of phosphors. Nevertheless, europium stands out among lanthanides due to its unique electronic transition and the distinctive magnetic dipole transition $^5D_0 \rightarrow {}^7F_1$. As a result, for phosphors doped with Eu^{3+}, the J-O parameters can be deduced from luminescence emission spectra instead [63]. In our investigation, we applied the Judd-Ofelt (J-O) theory to predict the luminescent characteristics of Eu^{3+} within the LBGW host. The J-O theory enables the determination of various parameters, including intensity parameters, branching ratio, radiative emission rates, lifetime, and asymmetric ratio. This theory was first introduced by Judd [64] and Ofelt [65]. It enables us to gain insights into the local environment and covalency of rare earth ions and lanthanide ions. J-O optical theory has been applied to study the potential mechanisms involved in the relaxation of trivalent lanthanide ions participating in host emission. It is widely employed to evaluate the spontaneous emission probability, denoted as $A(\Psi J \rightarrow \Psi J')$:

$$A(\Psi J \rightarrow \Psi J') = \frac{64\pi^4}{3h(2J+1)}\vartheta^3\left[\frac{n(n^2+2)^2}{9}D_{ED} + n^3 D_{MD}\right], \quad (8)$$

Here, ϑ represents the mean energy of the transition (measured in cm^{-1}), while h denotes the Planck constant (6.63×10^{-27} erg.s), and (2 J + 1) means a degeneration of the initial state. D_{ED} and D_{MD} refer to electrical and magnetic dipole forces respectively (measured in $esu^2\ cm^2$), the specific D_{MD} value given being $9.6 \times 10^{-42}\ esu^2\ cm^2$.

Additionally, n stands for the material's refractive index, with a given value of n = 2.00 [27]. Based on only three J-O phenomenological parameters, the strength of induced dipolar transitions is determined using the equation below:

$$D_{ED} = e^2 \sum_{\lambda=2,4,6} \Omega_\lambda \left[\langle \Psi J \| U^{(\lambda)} \| \Psi J' \rangle\right]^2, \quad (9)$$

where *e* represents the unit charge and $\left[\langle \Psi J \| U^{(\lambda)} \| \Psi J' \rangle\right]^2$ denotes the double-squared matrix element estimated in the intermediate coupling approximation. Typically, they are regarded as independent of the host material ($U^2 = 0.0032$, $U^4 = 0.0023$, $U^6 = 0.0002$), where U^2 states to the transition $^5D_0 \rightarrow {}^7F_2$, U^4 to the $^5D_0 \rightarrow {}^7F_4$ and U^6 to the $^5D_0 \rightarrow {}^7F_6$ transition). In this way, the J-O parameters of the intensity experiment can be computed from the ratio of the intensity of the $^5D_0 \rightarrow {}^7F_\lambda$ transitions (with λ = 2, 4 and 6), $\int I_\lambda(\vartheta)d\vartheta$, to the intensity of the $^5D_0 \rightarrow {}^7F_1$ transition, $\int I_1(\vartheta)d\vartheta$, as shown below:

$$\Omega_\lambda = \frac{D_{MD}}{e^2\vartheta_\lambda^3} \frac{9n^3\vartheta_1^3}{n(n^2+2)^2\left[\langle \Psi J \| U^{(\lambda)} \| \Psi J' \rangle\right]^2} \frac{\int I_\lambda(\vartheta)d\vartheta}{\int I_1(\vartheta)d\vartheta} \quad (10)$$

The 3 phenomenological intensity parameters, denoted as Ω_λ (where λ = 2, 4, and 6), which define the strength of induced electric dipole transitions in accordance with J–O theory [64,65], can be calculated using Eq.10.

This involves utilizing the reduced matrix element as reported by Carnall et al. [66,67]. Consequently, the Ω_λ parameters (for λ = 2, 4, and 6) can be individually assessed based on the emission transitions of $^5D_0 \rightarrow {}^7F_2$, $^5D_0 \rightarrow {}^7F_4$, and $^5D_0 \rightarrow {}^7F_6$, in turn [68]. Ω_2 is extremely dependent on the environment in which Eu^{3+} ions are found. As such, the maximum value of Ω_2 can be associated with changes in the structural environment around the Eu^{3+} ion given the hypersensitivity of the $^5D_0 \rightarrow {}^7F_2$ transition. The higher Ω_2 parameter is good evidence for the distorted symmetry of Eu^{3+}. The parameter Ω_4 is linked to the rigidity and durability of the matrix in which the rare earth ions are located. The intensity parameter Ω_6 was not established due to the experimental inability to detect the $^5D_0 \rightarrow {}^7F_6$ transition. The J-O intensity parameters, radiative transition probability for LBGW: *x* at.% Eu^{3+} phosphors are listed in Table 4 for the synthesized phosphor samples. In each instance, the dominance of the hypersensitive electric dipole transition is signified by Ω_2 surpassing Ω_4. The high Ω_2 parameter is attributed to the pronounced intensity of the $^5D_0 \rightarrow {}^7F_2$ transition in the PL spectra, highlighting the covalent nature of the Eu-O bond. The intensity parameter Ω_2 was found to be much larger than Ω_4 which indicates that the Eu^{3+} ions occupied in the low symmetry sites in the host lattice. The important value of Ω_2 reveals the weak symmetry around the europium ion. The calculation results support the above-mentioned structural discussion. The spontaneous emission probability $A(\Psi J \rightarrow \Psi J')$ for various transitions is related to the radiative lifetime τ_{rad} of an excited state ΨJ by the following relation:

$$\tau_{rad}(\Psi J) = \frac{1}{\sum A(\Psi J \rightarrow \Psi J')} \quad (11)$$

The fluctuations in the intensity of emission peaks can be elucidated

Table 4
Calculated probabilities of spontaneous radiative transitions of Eu^{3+} ions in LBGW phosphor[#].

Sample (at.%)	Transition $^5D_0 \rightarrow {}^7F_J$	υ cm^{-1}	J-O intensities Ω_2	Ω_4	A_{0J} (s^{-1})	β_{0J} (%)	A_R (s^{-1})	A_{NR} (s^{-1})	τ_{rad} (ms)	η(%)
1	$^7F_1^{MD}$	16,910	8.45	5.32	41.27	9.61	429.06	1221.74	2.33	26.00
	$^7F_2^{ED}$	16,259			332.09	77.39				
	$^7F_4^{ED}$	14,263			55.70	12.98				
2	$^7F_1^{MD}$	16,914	8.57	4.75	41.29	9.71	424.95	1239.56	2.35	25.53
	$^7F_2^{ED}$	16,260			329.86	77.62				
	$^7F_4^{ED}$	14,263			53.80	12.66				
3	$^7F_1^{MD}$	16,915	9.53	4.56	41.30	9.96	414.53	1258.98	2.41	26.35
	$^7F_2^{ED}$	16,259			321.56	77.57				
	$^7F_4^{ED}$	14,262			51.63	12.45				
4	$^7F_1^{MD}$	16,918	9.96	4.21	41.33	9.33	442.82	1237.71	2.25	26.01
	$^7F_2^{ED}$	16,260			341.10	77.02				
	$^7F_4^{ED}$	14,264			60.39	13.63				
5	$^7F_1^{MD}$	16,909	10.25	4.07	41.26	9.33	442.14	1243.48	2.26	26.23
	$^7F_2^{ED}$	16,254			343.93	77.78				
	$^7F_4^{ED}$	14,264			56.95	12.88				
7	$^7F_1^{MD}$	16,907	11.69	3.95	41.25	9.62	428.49	1290.28	2.33	24.93
	$^7F_2^{ED}$	16,259			329.89	76.98				
	$^7F_4^{ED}$	14,261			57.38	13.39				
10	$^7F_1^{MD}$	16,913	11.98	3.66	41.29	9.56	443.70	1299.03	2.25	25.46
	$^7F_2^{ED}$	16,260			343.81	76.83				
	$^7F_4^{ED}$	14,264			58.60	13.45				

#υ-wavenumber of the emission band, A_{0J} – probability of radiative spontaneous transition, A_R– Radiative transition rate, A_{NR}– Non-radiative transition rate, B_{0J} – luminescence branching ratio, τ_{rad} –the radiative lifetime of the excited state, respectively, ED and MD stand for the electric-dipole and magnetic-dipole contributions, respectively.

by selective rules, which are also responsible for the disparities in branching ratio values. The branching ratio evaluates the proportion of emission for a particular transition of a state relative to all other transitions originating from that state. We derive the fluorescence branching ratio, denoted β(ΨJ → ΨJ'), based on the radiative decay rates using the expression:

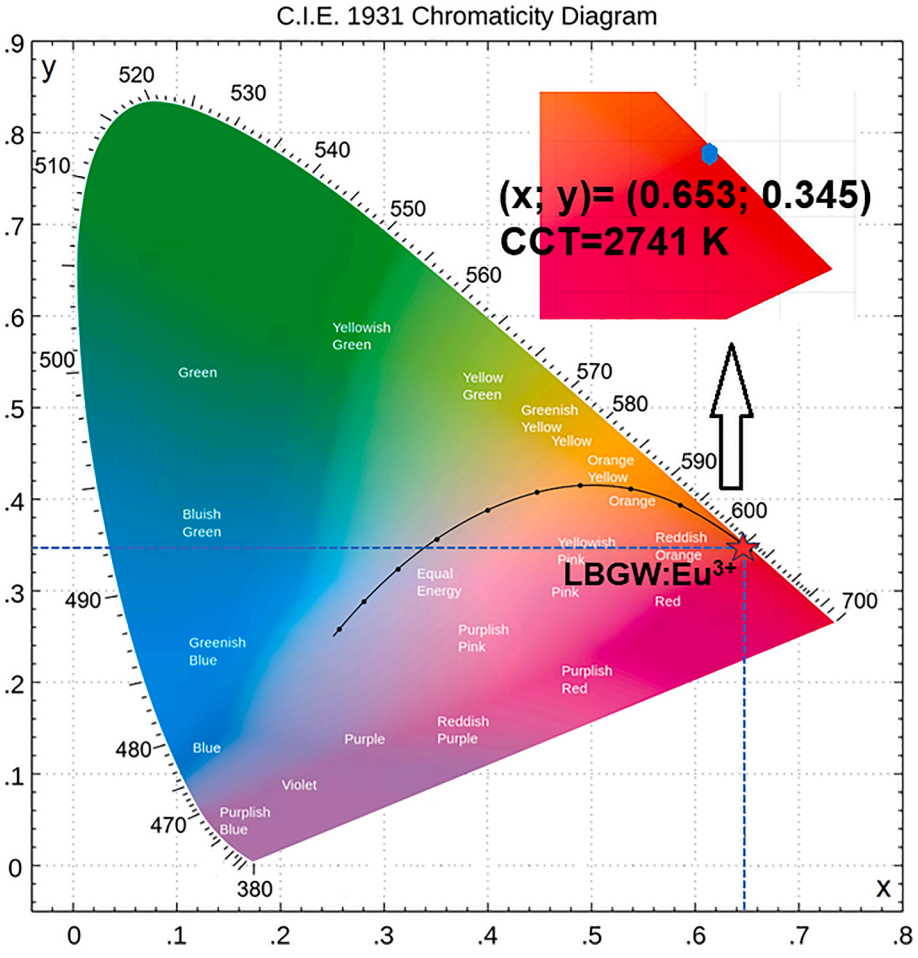

Fig. 11. CIE chromaticity diagram of LBGW: 3 at.% Eu^{3+} phosphor.

$$\beta(\Psi J \rightarrow \Psi J') = \frac{A(\Psi J \rightarrow \Psi J')}{\sum A(\Psi J \rightarrow \Psi J')} = \tau_{rad} A(\Psi J \rightarrow \Psi J'), \quad (12)$$

where

$$A(\Psi 0 \rightarrow \Psi 1) = \frac{64\pi^4 \vartheta^3 n^3}{3h(2J+1)} D_{MD}, \quad (13)$$

$$A(\Psi 0 \rightarrow \Psi J) = A_{J1} A(\Psi 0 \rightarrow \Psi 1), \quad (14)$$

The experimental decay lifetime τ_{lum} is contrasted with the theoretically calculated lifetime determined using J–O theory. The difference between the calculated and the experimental values may be attributed to non-radiative decay of the $^5D_0$ state of Eu^{3+} ions. The computed value of the quantum efficiency can be evaluated by the following expression:

$$\eta = \frac{A_R}{A_R + A_{NR}} = \frac{\tau_{lum}}{\tau_{rad}(\Psi J)}, \quad (15)$$

The quantum efficiency reveals the highest value for LBGW: 3 at. % Eu^{3+} and it is $\eta = 26.35$ %. The reduction in quantum efficiency beyond a doping concentration of 5 atomic percent is attributed to elevated cross-relaxation processes. Such quantum efficiency indicates possibility of the use of $Li_3Ba_2Gd_3(WO_4)_8$: Eu^{3+} in solid state lighting application.

3.7. CIE chromaticity coordinate analysis

By applying the colour matching functions $\bar{x}(\lambda)$, $\bar{y}(\lambda)$, $\bar{z}(\lambda)$ given by the International Commission on Illumination1931 (CIE), the chromaticity coordinates (x, y) can be determined based on the spectral emission data of the phosphor [69]. The coordinates (x, y) shown on a chromaticity diagram are used to specify the colour of the light source. Fig. 11 describes the CIE chromaticity diagram of LBGW phosphor doped with 3 % Eu^{3+} at 395 nm excitation. The colour coordinates of this sample were defined as (0.653, 0.345) in the red region, near those of standard red light (0.670, 0.330).

The correlated colour temperature (CCT) parameter is evaluated using the Planck locus. This is just one part of the chromaticity diagram (x, y) and a wide range of operating points exist outside the Planck locus. When the light source coordinates are not situated on the Planck locus, CCT is used to determine the colour temperature of a light source. In addition, white light quality in terms of CCT was provided by McCamy's empirical relationship [70]:

$$CCT = -437n^3 + 3601n^2 - 6861n + 5514.31, \quad (16)$$

where $n = \frac{x - x_e}{y - y_e}$, $x_e = 0.332$; $y_e = 0.186$ refer to the coordinates of the epicenter of the convergence and n is the inverse slope line. The purity of colour emitted by this sample was computed based on the following equation [71]:

$$Colourpurity = \frac{\sqrt{(x - x_{ee})^2 + (y - y_{ee})^2}}{\sqrt{(x_d - x_{ee})^2 + (y_d - y_{ee})^2}} \times 100\%, \quad (17)$$

Here, (x, y) represent the color coordinates of the phosphor, (x_{ee}, y_{ee}) correspond to the coordinates of the CIE 1931 standard source, and (x_d, y_d) indicate the color coordinates of the dominant wavelength. This can be determined by extending a straight line between the point (x, y) and the illumination point on the other side. Color purity calculated for LBGW: 3 at.% Eu^{3+} phosphors, when excited with a wavelength of 395 nm, stands at 98.42 %. This high value signifies a distinctly pure red emission from LBGW: Eu^{3+}. These results also indicate that the LBGW phosphors activated by Eu^{3+} display admirable CIE color coordinates and remarkably high color purity. The produced phosphors show significant promise for use in white LEDs as red-emitting phosphors when exposed to UV light. The calculated CIE coordinates and CCT values are detailed in Table 5, corresponding to the emission spectra recorded at $\lambda_{exc} = 395$ nm for LBGW phosphors doped with Eu^{3+} at concentrations ranging from 0.5 to 10 at.%.

Table 5
CIE coordinates, CCT and color purity of the prepared LBGW: x at.% Eu^{3+} samples.

Eu^{3+} concentration (at.%)	x	y	CCT	Color purity
0.5	0.657	0.341	2937	97.10
1	0.656	0.342	2884	97.50
2	0.654	0.344	2789	98.09
3	0.653	0.345	2741	98.42
4	0.655	0.342	2857	98.51
5	0.656	0.341	2901	98.64
7	0.654	0.343	2813	98.71
10	0.660	0.338	3063	98.96

3.8. Thermal stability

The thermal resilience of a phosphor stands as a crucial factor in its potential application in high-power wLEDs. Fig. 12(a) shows the photoluminescence (PL) spectra of LBGW: 3 at.% Eu^{3+} phosphors when excited at 395 nm, recorded at various temperatures ranging from 30 °C

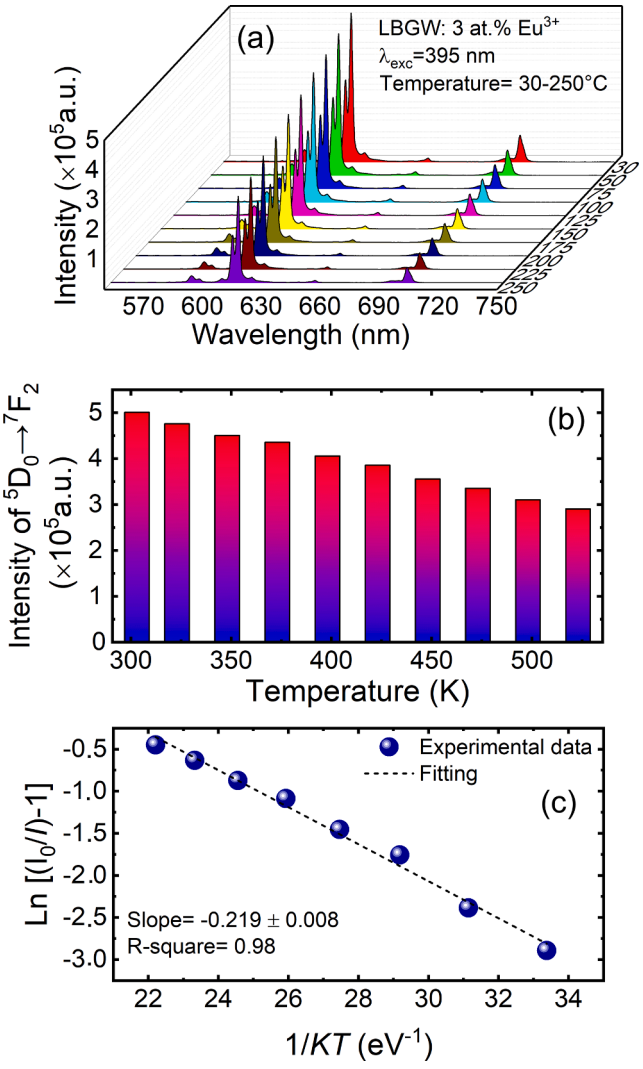

Fig. 12. (a) Emission spectra of the prepared LBGW: 3 at.%Eu^{3+} phosphors measured at various temperatures; (b) Evolution of the intensity of $^5D_0 \rightarrow {}^7F_2$ transition as function of the temperature; (c) The relationship of ln[(I_0/I]-1) versus 1/kT of LBGW: 3 at.%Eu^{3+} phosphors.

to 250 °C. This measurement clearly illustrate that an elevation in temperature results in a decrease in PL intensity, attributed to the phenomenon of thermal quenching. Essentially, the PL intensity of the phosphors at 423 K, compared to that at room temperature, serves as a measure of the phosphor's efficiency. It is noted that the PL intensities at 423 K decrease to approximately 79.5 % of their initial value at room temperature, as shown in Fig. 12(b). To gain a more profound understanding of the temperature's influence on the PL intensity of the synthesized phosphors, the activation energy is calculated using the Arrhenius equation, as presented below [40]:

$$I(T) = \frac{I_0}{1 + c\exp(-\frac{\Delta E_a}{KT})}, \tag{18}$$

where $I(T)$ denotes the PL intensity at different given temperature (T), While I_0 is the initial PL intensity, ΔE_a represents the activation energy for thermal quenching, K is known as Boltzmann's constant (8.629×10^{-5} eV K^{-1}), and c is a constant for the host phosphor. To estimate the value of ΔE_a, equation (19) is modified by equation (18) as shown below [72]:

$$\ln\left[\left(\frac{I_0}{I}\right) - 1\right] = -\frac{\Delta E_a}{KT} + lnc, \tag{19}$$

Plotting ln [(I_0/I)-1] against 1/kT produced a straight line, Fig. 12(c). The fitted line has a slope of approximately −0.219 and thus the activation energy (ΔE_a) for the LBGW: 3 at.% Eu^{3+} phosphor is 0.219 eV. This value is lower than that of other Eu^{3+} activated quaternary tungstate phosphors such as $Li_3Ba_2Y_3(WO_4)_8$: 0.27 eV [51], $Li_3Ba_2La_3(WO_4)_8$: 0,24 eV [73] and $Li_3BaSrLa_3(WO_4)_8$: 0,30 eV [36].

4. Conclusion

In summary, we successfully synthesized red-emitting phosphors by incorporating varying concentrations of Eu^{3+} into LBGW ($0.5 \leq x \leq 10$) using the solid-state reaction method. XRD was used to characterize the structure of these phosphors, DTA, Raman analysis, and SEM microscopy. Upon excitation at an ultraviolet wavelength of 395 nm, the developed phosphors emitted red light with a peak at 614 nm, corresponding to the $^5D_0 \rightarrow {}^7F_2$ electric dipolar transition of Eu^{3+} ions. The optimal concentration of Eu^{3+} in LBGW: x at.% Eu^{3+} phosphors was determined to be x = 3. Concentration quenching was attributed to dipole-quadrupole interactions, with a critical energy transfer distance between Eu^{3+} ions calculated at 7.409 Å. J-O theory analysis confirmed the non-centrosymmetric arrangement of the activator ion. Additionally, fluorescence decay lifetimes were examined. Furthermore, the color coordinates for LBGW: 3 at.% Eu^{3+} were determined as (0.653, 0.345) with nearly perfect color purity. The activation energy for the transition from the $^5D_0$ state to the CTB state was determined to be 0.219 eV, highlighting the remarkable thermal stability of our phosphor. These synthesized LBGW: Eu^{3+} phosphors exhibit potential as materials emitting red light for white LEDs pumped by near-UV. We anticipate that this research will inspire future advancements in other LBGW phosphors and single crystals doped with various RE^{3+} ions such as Sm^{3+}, Yb^{3+}, and Tm^{3+} providing visible and near-IR emissions and finding applications in solid-state lighting and lasers.

CRediT authorship contribution statement

Zhonghuan Zhang: Writing – original draft, Investigation. **Abir Douzi:** Writing – original draft, Software, Methodology, Investigation, Data curation. **Sami Slimi:** Writing – review & editing, Writing – original draft, Software, Methodology, Investigation, Conceptualization. **Eduard Madirov:** Writing – review & editing, Investigation. **Amal Arouri:** Investigation. **Víctor Llamas:** Investigation. **Josep Maria Serres:** Writing – review & editing, Investigation. **Rosa Maria Solé:** Writing – review & editing. **Magdalena Aguiló:** Writing – review & editing, Resources, Funding acquisition. **Francesc Díaz:** Writing – review & editing, Resources, Funding acquisition. **Ezzedine Ben Salem:** Writing – review & editing. **Andrey Turshatov:** Writing – review & editing, Validation, Investigation, Conceptualization. **Bryce S. Richards:** Writing – review & editing, Resources, Funding acquisition. **Xavier Mateos:** Writing – review & editing, Validation, Supervision, Funding acquisition, Conceptualization.

Declaration of competing interest

The authors declare that they have no known competing financial interests or personal relationships that could have appeared to influence the work reported in this paper.

Data availability

No data was used for the research described in the article.

Acknowledgements

This research article has been possible with the support of the Secretaria d'Universitats i Recerca del Departament d'Empresa i Coneixement de la Generalitat de Catalunya, the European Union (UE), and the European Social Fund (ESF) (2022 FI_B1 00021). Grants PID2022-141499OB-I00 and PID2019-108543RB-I00 funded by MCIN/AEI/10.13039/501100011033. The financial support provided by the Helmholtz Association is gratefully acknowledged: (i) a Recruitment Initiative Fellowship for B.S.R.; (ii) the funding of chemical synthesis equipment from the Helmholtz Materials Energy Foundry (HEMF); and (iii) Research Field Energy – Program Materials and Technologies for the Energy Transition – Topic 1 Photovoltaics.

References

[1] S. Neeraj, N. Kijima, A.K. Cheetham, Novel red phosphors for solid-state lighting: the system NaM(WO4)2–x(MoO4)x: Eu3+ (M=Gd, Y, Bi), Chem. Phys. Lett. 387 (2004) 2–6.
[2] H. Zhou, Q. Wang, M. Jiang, X. Jiang, Y. Jin, A novel green-emitting phosphor Ba2Gd2Si4O13: Eu2+ for near UV-pumped light-emitting diodes, Dalt. Trans. 44 (2015) 13962–13968.
[3] X. Gao, Y. Wang, D. Wang, B. Liu, Luminescent properties of KGd1− x(WO4)2: Eux3+ and KGd1− x(WO4)2− y(MoO4)y: Eux3+ phosphors in UV–VUV regions, J. Lumin. 129 (2009) 840–843.
[4] X. Ding, Q. Wang, Y. Wang, Rare-earth-free red-emitting K2Ge4O9: Mn4+ phosphor excited by blue light for warm white LEDs, Phys. Chem. Chem. Phys. 18 (2016) 8088–8097.
[5] M. Chen, Z. Xia, Q. Liu, Luminescence properties and energy transfer of Ce3+/Tb3+ co-doped Ca6Ba(PO4)4O phosphor for near-UV pumped light-emitting diodes, J. Mater. Chem. C. 3 (2015) 4197–4204.
[6] M. Shang, C. Li, J. Lin, How to produce white light in a single-phase host? Chem. Soc. Rev. 43 (2014) 1372–1386.
[7] J.C.G. Bünzli, C. Piguet, Taking advantage of luminescent lanthanide ions, Chem. Soc. Rev. 34 (2005) 1048–1077.
[8] V.B. Pawade, H.C. Swart, S.J. Dhoble, Review of rare earth activated blue emission phosphors prepared by combustion synthesis, Renew. Sustain. Energy Rev. 52 (2015) 596–612.
[9] A. Tiwari, S.J. Dhoble, Tunable lanthanide/transition metal ion-doped novel phosphors for possible application in w-LEDs: a review, Luminescence. 35 (2020) 4–33.
[10] M. Kim, S.P. Singh, S. Shim, W.B. Park, K.-S. Sohn, Discovery of a Quaternary Sulfide, Ba2–x LiAlS4: Eu2+, and Its Potential as a Fast-Decaying LED Phosphor, Chem. Mater. 32 (2020) 6697–6705.
[11] C. Li, X.-M. Wang, Z.-P. Yang, H. Jiao, Ca8Mg7Si9N22: Ce3+—a yellow-emitting nitride phosphor for white light emitting diodes, ACS Appl. Electron. Mater. 2 (2020) 936–943.
[12] R. Cao, X. Lv, Y. Jiao, Y. Ran, S. Guo, H. Ao, T. Chen, T. Fan, Ca3La6Si6O24:Eu3+ orange-red-emitting phosphor: Synthesis, structure and luminescence properties, Mater. Res. Bull. 122 (2020) 110651.
[13] Z. Zhang, L. Sun, B. Devakumar, G. Annadurai, J. Liang, S. Wang, Q. Sun, X. Huang, Synthesis and photoluminescence properties of a new blue-light-excitable red phosphor Ca2LaTaO6: Eu3+ for white LEDs, J. Lumin. 222 (2020) 117173.
[14] B. Yu, Y. Li, R. Zhang, H. Li, Y. Wang, A novel thermally stable eulytite-type NaBaBi2(PO4)3: Eu3+ red-emitting phosphor for pc-WLEDs, J. Alloys Compd. 852 (2021) 157020.

[15] Y. Hua, W. Ran, J.S. Yu, Excellent photoluminescence and cathodoluminescence properties in Eu3+-activated Sr2LaNbO6 materials for multifunctional applications, Chem. Eng. J. 406 (2021) 127154.
[16] R. Cao, H. Liang, T. Chen, Z. Wu, Z. Jiang, X. Yi, J. Wen, Q. Zhong, Study on luminescence characterizations of SrMg2La2W2O12:Eu3+ red-emitting phosphor, J. Phys. Chem. Solids. 163 (2022) 110569.
[17] W. Ye, C. Zhao, X. Shen, C. Ma, Z. Deng, Y. Li, Y. Wang, C. Zuo, Z. Wen, Y. Li, High quantum yield Gd4. 67Si3O13: Eu3+ red-emitting phosphor for tunable white light-emitting devices driven by UV or blue LED, ACS Appl, Electron. Mater. 3 (2021) 1403–1412.
[18] E. Ezerskyte, J. Grigorjevaite, A. Minderyte, S. Saitzek, A. Katelnikovas, Temperature-dependent luminescence of red-emitting Ba2Y5B5O17: Eu3+ phosphors with efficiencies close to unity for near-UV LEDs, Materials (basel). 13 (2020) 763.
[19] S. Wang, C. Xu, X. Qiao, High thermal stability and color purity of red-emitting phosphor Y2SiWO8: Eu3+ for w-LEDs: synthesis and photoluminescence properties, Ceram. Int. 47 (2021) 1063–1075.
[20] S. Wang, Y. Xu, T. Chen, W. Jiang, J. Liu, X. Zhang, W. Jiang, L. Wang, A red phosphor LaSc3(BO3)4: Eu3+ with zero-thermal-quenching and high quantum efficiency for LEDs, Chem. Eng. J. 404 (2021) 125912.
[21] R. Krishnan, R.E. Kroon, H.C. Swart, Charge transfer characteristics and luminescence properties of Eu3+ activated Ba2YMoO6 and BaY2(MoO4)4 phosphors, Mater. Res. Bull. 145 (2022) 111554.
[22] X. Shi, Z. Wang, T. Takei, X. Wang, Q. Zhu, X. Li, B.-N. Kim, X. Sun, J.-G. Li, Selective crystallization of four tungstates (La2W3O12, La2W2O9, La14W8O45, and La6W2O15) via hydrothermal reaction and comparative study of Eu3+ luminescence, Inorg. Chem. 57 (2018) 6632–6640.
[23] X. Li, H. Xu, X. Xia, F. Xie, S. Zhong, D. Xu, One-step synthesis of Sc2W3O12: Eu3+ phosphors with tunable luminescence for WLED, Ceram. Int. 45 (2019) 10461–10467.
[24] B. Bondzior, T.H.Q. Vu, D. Stefańska, M.J. Winiarski, P.J. Dereń, Tunable broadband emission by bandgap engineering in (Ba, Sr)2(Mg, Zn)WO6 inorganic double-perovskites, J. Alloys Compd. 888 (2021) 161567.
[25] E. Sreeja, S. Gopi, V. Vidyadharan, P.R. Mohan, C. Joseph, N.V. Unnikrishnan, P. R. Biju, Luminescence properties and charge transfer mechanism of host sensitized Ba2CaWO6: Eu3+ phosphor, Powder Technol. 323 (2018) 445–453.
[26] G. Fan, X. Wang, X. Qiu, D. Fan, R. Hu, Z. Tian, Luminescent properties of orange-red emitting phosphors NaGd(MoO4)(WO4): Sm3+ for white LED, Opt. Mater. (amst) 91 (2019) 363–370.
[27] H. Li, L. Zhang, G. Wang, Growth, structure and spectroscopic characterization of a new laser crystals Nd3+:Li3Ba2Gd3(WO4)8, J. Alloys Compd. 478 (2009) 484–488.
[28] A. Douzi, S. Slimi, E. Madirov, A. Turshatov, B.S. Richards, R.M. Solé, M. Aguiló, F. Díaz, E. Ben Salem, X. Mateos, Structure and luminescence properties of Dy3+ doped quaternary tungstate Li3Ba2Gd3(WO4)8 for application in wLEDs, RSC Adv. 13 (2023) 23772–23787.
[29] W.L. Guo, Y.T. Jiao, P.S. Wang, Q. Liu, S. Liu, F. Hou, Energy transfer and spectroscopic characterization of new green emitting $li_3ba_2Gd_3(Wo_4)_8:Tb^{3+}$ phosphor, Solid State Phenom. 281 SSP (2018) 686–691.
[30] Y. Zhao, Y. Huang, L. Zhang, Z. Lin, G. Wang, Growth and spectral properties of Er3+/Yb3+: Li3Ba2Gd3(WO4)8 crystal, Optoelectron. Adv. Mater. Commun. 6 (2012) 357–362.
[31] R.D. Shannon, Revised effective ionic radii and systematic studies of interatomic distances in halides and chalcogenides, Acta Crystallogr, Sect. A Cryst. Physics, Diffraction, Theor. Gen. Crystallogr. 32 (1976) 751–767.
[32] J. Dalal, A. Khatkar, M. Dalal, S. Chahar, P. Phogat, V.B. Taxak, S.P. Khatkar, Ba2YV3O11: Eu3+– Density functional and experimental analysis of crystal, electronic and optical properties, J. Alloys Compd. 821 (2020) 153471.
[33] L. Macalik, J. Hanuza, A.A. Kaminskii, Polarized Raman spectra of the oriented NaY(WO4)2 and KY(WO4)2 single crystals, J. Mol. Struct. 555 (2000) 289–297.
[34] L. Macalik, J. Hanuza, A.A. Kaminskii, Polarized infrared and Raman spectra of KGd(WO4)2 and their interpretation based on normal coordinate analysis, J. Raman Spectrosc. 33 (2002) 92–103.
[35] B. Han, J. Zhang, Z. Wang, Y. Liu, H. Shi, Investigation on the concentration quenching and energy transfer of red-light-emitting phosphor Y_2MoO_6: Eu^{3+}, J. Lumin. 149 (2014) 150–154.
[36] K. Singh, S. Vaidyanathan, Li3BaSrLa3(WO4)8: Eu3+ and Its Solid Solutions: A New Red Emitting Phosphor-Structure, Synthesis and Appraisal of Optical Properties, ChemistrySelect. 2 (2017) 5143–5156.
[37] E.A. Davis, Nf. Mott, Conduction in non-crystalline systems V. Conductivity, optical absorption and photoconductivity in amorphous semiconductors, Philos. Mag. 22 (1970) 903–922.
[38] K.K. Rasu, S.M. Babu, Impact of Eu3+ concentration on the fluorescence properties of the LiGd (W0. 5Mo0. 5O4)2 novel red phosphors, Solid State Sci. 98 (2019) 106028.
[39] D.L. Shruthi, A.J. Reddy, G.N.A. Kumar, C.K. Jayasankar, Judd Ofelt theoretical analysis, Photoluminescence properties of Eu3+activated LiGd(WO4)2 phosphors, J. Lumin. 222 (2020) 117167.
[40] H. Guo, X. Huang, Y. Zeng, Synthesis and photoluminescence properties of novel highly thermal-stable red-emitting Na3Sc2(PO4)3:Eu3+ phosphors for UV-excited white-light-emitting diodes, J. Alloys Compd. 741 (2018) 300–306.
[41] R. Guo, S. Tang, B. Cheng, D. Tan, A new red emitting phosphor: $La_2SrB_{10}O_{19}$: Eu^{3+}, J. Lumin. 138 (2013) 170–173.
[42] H.-Y. Chen, H.-L. Lai, R.-Y. Yang, S.-J. Chang, Effect of different alkali carbonate on the microstructure and photoluminescent properties of YInGe2O7: Eu3+ phosphors, J. Mater. Sci. Mater. Electron. 27 (2016) 2963–2967.
[43] Y. Shi, B. Liu, C. Li, W. Luo, Z. Wang, Effect of W6+ dopant on the morphology and luminescence properties of NaLa(MoO4)2: Eu3+ phosphors, Mater. Res. Bull. 101 (2018) 319–323.
[44] G. Li, Y. Wei, W. Long, G. Xu, Photoluminescence properties, energy transfer and thermal stability of the novel red-emitting CaGd2(WO4)4:Eu3+, Sm3+ phosphors, Mater. Res. Bull. 95 (2017) 86–94.
[45] P. Jiang, W. Gao, R. Cong, T. Yang, Structural investigation of the A-site vacancy in scheelites and the luminescence behavior of two continuous solid solutions A1–1.5xEux□0.5xWO4 and A0.64-0.5yEu0.24Liy□0.12-0.5yWO4 (A = Ca, Sr; □ = vacancy), Dalt. Trans. 44 (2015) 6175–6183.
[46] Y. Su, L. Li, G. Li, P. Li, G. Li, L. Li, G. Li, P. Li, G. Li, Synthesis and optimum luminescence of CaWO4-based red phosphors with codoping of Eu3+ and Na+, Chem. Mater. 20 (2008) 6060–6067.
[47] W.C. Nieuwpoort, G. Blasse, Linear crystal-field terms and the 5Do - 7Fo transition of the Eu3+ ion, Solid State Commun. 4 (1966) 227–229.
[48] M. Xia, Z. Ju, H. Yang, Z. Wang, X. Gao, F. Pan, W. Liu, Red-emitting enhancement by inducing lower crystal field symmetry of Eu3+ site in CaWO4:Eu3+ phosphor for n-UV w-LEDs, J. Alloys Compd. 739 (2018) 439–446.
[49] S. Shi, X. Liu, J. Gao, J. Zhou, Spectroscopic properties and intense red-light emission of (Ca, Eu, M)WO_4 (M = Mg, Zn, Li), Spectrochim. Acta - Part A Mol. Biomol. Spectrosc. 69 (2008) 396–399.
[50] B.P. Singh, J. Singh, R.A. Singh, Luminescence properties of Eu3+-activated SrWO4 nanophosphors-concentration and annealing effect, RSC Adv. 4 (2014) 32605–32621.
[51] L. Wang, W. Guo, Y. Tian, P. Huang, Q. Shi, High luminescent brightness and thermal stability of red emitting Li3Ba2Y3(WO4)8: Eu3+ phosphor, Ceram. Int. 42 (2016) 13648–13653.
[52] D.L. Dexter, J.H. Schulman, Theory of concentration quenching in inorganic phosphors, J. Chem. Phys. 22 (1954) 1063–1070.
[53] C.-H. Chiu, C.-H. Liu, S.-B. Huang, T.-M. Chen, Synthesis and luminescence properties of intensely red-emitting M5Eu(WO4)4–x(MoO4) x (M= Li, Na, K) phosphors, J. Electrochem. Soc. 155 (2008) J71.
[54] G. Blasse, Energy transfer between inequivalent Eu2+ ions, J. Solid State Chem. 62 (1986) 207–211.
[55] D. Dl, D.L. Dexter, A theory of sensitized luminescence in solids, J. Chem. Phys. 21 (1953) 836–850.
[56] L.G. Van Uitert, Characterization of Energy Transfer Interactions between Rare Earth Ions, J. Electrochem. Soc. 114 (1967) 1048.
[57] I.E. Kolesnikov, A.V. Povolotskiy, D.V. Mamonova, E.Y. Kolesnikov, A. V. Kurochkin, E. Lähderanta, M.D. Mikhailov, Asymmetry ratio as a parameter of Eu3+ local environment in phosphors, J. Rare Earths. 36 (2018) 474–481.
[58] T.L. Francis, P.P. Rao, M. Thomas, S.K. Mahesh, V.R. Reshmi, Effect of Zr4+ and Si4+ substitution on the luminescence properties of CaMoO 4: Eu3+ red phosphors, J. Mater. Sci. Mater. Electron. 25 (2014) 2387–2393.
[59] Y. Zhang, W. Gong, G. Ning, Novel red-emitting LiGd(WO4)2: Eu3+ phosphor with high thermal stability and high color purity for application in white light-emitting diodes, New J. Chem. 40 (2016) 10136–10143.
[60] A. Fu, A. Guan, F. Gao, X. Zhang, L. Zhou, Y. Meng, H. Pan, A novel double perovskite La2ZnTiO6: Eu3+ red phosphor for solid-state lighting: synthesis and optimum luminescence, Opt. Laser Technol. 96 (2017) 43–49.
[61] J. Grigorjevaite, A. Katelnikovas, Luminescence and luminescence quenching of K2Bi (PO4)(MoO4): Eu3+ phosphors with efficiencies close to unity, ACS Appl. Mater. Interfaces. 8 (2016) 31772–31782.
[62] L.I. Mengting, J. Baoxiang, Synthesis and photoluminescence properties of ZnTiO3: Eu3+ red phosphors via sol-gel method, J. Rare Earths. 33 (2015) 231–238.
[63] C. Görller-Walrand, L. Fluyt, A. Ceulemans, W.T. Carnall, Magnetic dipole transitions as standards for Judd-Ofelt parametrization in lanthanide spectra, J. Chem. Phys. 95 (1991) 3099–3106.
[64] B.R. Judd, Configuration interaction in rare earth ions, Proc. Phys. Soc. 82 (1963) 874.
[65] G.S. Ofelt, Intensities of crystal spectra of rare-earth ions, J. Chem. Phys. 37 (1962) 511–520.
[66] W.T. Carnall, P.R. Fields, K. Rajnak, Electronic energy levels in the trivalent lanthanide aquo ions. I. Pr^{3+}, Nd^{3+}, Pm^{3+}, Sm^{3+}, Dy^{3+}, Ho^{3+}, Er^{3+}, and Tm^{3+}, J. Chem. Phys. 49 (1968) 4424–4442.
[67] W.T. Carnall, Optical spectroscopy of f-element compounds, in: Organometallics F-Elements Proc. NATO Adv. Study Inst. Held Sogesta, Urbino, Italy, Sept. 11–22, 1978, Springer, 1979: pp. 281–307.
[68] B. Peng, T. Izumitani, The Fluorescence Properties of Eu3+ in Various Glasses and the Energy Transfer Between Eu3+ and Sm3+ in Borosilico-phosphate Glass, Rev. Laser Eng. 22 (1994) 16–27.
[69] H.-J. Woo, S. Gandhi, M. Jayasimhadri, D.-S. Shin, H.S. Lee, K. Jang, Engendering color tunable emission in calcium silicate based phosphors via ageing of silicate source, Sensors Actuators B Chem. 241 (2017) 1106–1110.
[70] C.S. McCamy, Correlated color temperature as an explicit function of chromaticity coordinates, Color Res. Appl. 17 (1992) 142–144.
[71] Y.-C. Fang, S.-Y. Chu, P.-C. Kao, Y.-M. Chuang, Z.-L. Zeng, Energy transfer and thermal quenching behaviors of CaLa2(MoO4)4: Sm3+, Eu3+ red phosphors, J. Electrochem. Soc. 158 (2010) J1.
[72] X. Huang, B. Li, H. Guo, Highly efficient Eu3+-activated K2Gd (WO4)(PO4) red-emitting phosphors with superior thermal stability for solid-state lighting, Ceram. Int. 43 (2017) 10566–10571.
[73] J. Hu, X. Gong, J. Huang, Y. Chen, Y. Lin, Z. Luo, Y. Huang, Near ultraviolet excited Eu3+ doped Li3Ba2La3(WO4)8 red phosphors for white light emitting diodes, Opt. Mater. Express. 6 (2016) 181–190.